Atomization and Sprays, 23 (5): 419–442 (2013)

LARGE EDDY SIMULATION OF HIGH-VELOCITY FUEL SPRAYS: STUDYING MESH RESOLUTION AND BREAKUP MODEL EFFECTS FOR SPRAY A

A. Wehrfritz,* V. Vuorinen, O. Kaario, & M. Larmi

Aalto University, School of Engineering, Finland

*Address all correspondence to A. Wehrfritz E-mail: armin.wehrfritz@aalto.fi

Large eddy simulation (LES) of the nonreacting Spray A target conditions, as defined by the Engine Combustion Network, are carried out and compared to high-quality, experimental validation data. The investigated test case is characterized by a high injection pressure, small nozzle hole diameter, and inert ambient gas conditions at high-temperature and high-pressure. In the present study, implicit LES is used together with the Lagrangian particle tracking approach for the liquid phase to (i) investigate the effect of mesh resolution and (ii) study the influence of droplet breakup modeling on the local and global flow characteristics. Two breakup models are compared at four different mesh resolutions. The results are quantitatively analyzed with respect to integral spray quantities and validated against the experimental data. Qualitative characterization of the local velocities and mixture formation is presented. A good agreement of simulated and measured liquid/vapor penetration is achieved for both breakup models, given a sufficient mesh resolution. However, local differences in droplet diameter and vapor mass are observed between the breakup models in the nozzle vicinity. The overall mixture formation shows little dependency on the breakup modeling approach yet a strong dependency on the mesh resolution.

KEY WORDS: *large eddy simulation, high-velocity fuel sprays, droplet breakup modeling, mesh resolution*

1. INTRODUCTION

Sprays have a fundamental role in internal combustion engine applications. Because the automotive industry is driven by the demand for lower emissions and higher fuel efficiency, fuel sprays become important in combustion optimization. Particularly, a deeper understanding of the processes and phenomena related to the liquid–gas phase interaction is crucial because it is the first step in the mixture formation. Besides experimental studies, 3D flow simulations offer a versatile tool to investigate these processes in detail. However, the methods and models used in such simulations impose their own challenges, especially with an increasing demand for more accurate results. Hence high-quality, quantitative experimental data are needed in order to develop and to validate

1044–5110/13/$35.00

high-fidelity multiscale computational models. A joint effort of several international research groups, the Engine Combustion Network (ECN) (2012), aims at providing such data sets for diesel fuel sprays. The first target conditions, called Spray A, have been defined by Pickett et al. (2010), and recent efforts aim at more detailed boundary condition characterization [e.g., Meijer et al. (2012); Payri et al. (2012a,b)].

In the present work, Spray A is used as a reference case to investigate the performance of certain computational models for high-velocity fuel sprays. Traditionally, computational fluid Dynamic (CFD) simulations of turbulent flows have been carried out using the Reynolds-averaged Navier-Stokes (RANS) approach. In RANS simulations, all scales of turbulence are modeled and the results can be seen as a time-averaged description of the flow field. The Large eddy simulation (LES) approach leads to a higher degree of detail, which is obtained by simulating the large scales of turbulence directly. LES still requires the modeling of the small scales, whereas direct numerical simulation (DNS) resolves the whole turbulence spectrum directly and delivers the most accurate results. The main computational concepts for spray simulations are the Lagrangian particle tracking (LPT) and the Euler-Euler (E-E) methods (Stiesch, 2003). Where the latter treats both the gaseous and liquid phase as continua, the LPT method assumes the liquid phase as discrete particles. The E-E method is well suited for dense sprays as they occur in the near nozzle region of typical fuel sprays, whereas the LPT method is better suited for dilute spray regions. Because typical fuel sprays are characterized by a very short liquid core and fast atomization due to hot air entrainment, sprays become quickly dilute and evaporate fast (Siebers, 1998). Hence, the present study applies the LPT concept together with the LES approach for fuel spray simulation.

Alternative spray models have been proposed by Abraham and Magi (1999); Iyer and Abraham (1997) have shown that gas jets with the same orifice mass and momentum flow rate as the spray are able to predict the vapor penetration and spreading reasonably well. A comparative study of these models was given by Abraham and Pickett (2010), who provided a picture of the spatial fuel vapor distribution. Leveraging the similarities between gas jets and dilute sprays, Vuorinen et al. (2010a,b) investigated Stokes number effects and spray formation by simulating a particle laden jet. Assuming complete atomization when far enough from the injector, Vuorinen et al. (2011) proposed a simplified model to take droplet breakup at lower Weber numbers into account. LES of particle laden flows and sprays using LPT have been presented by Bharadwaj and Rutland (2010), who studied subgrid two-phase interaction. An improved modeling of the subgrid kinetic energy was found by introducing a particle source term to the gas-phase transport equation. In a study by Kitaguchi et al. (2012), breakup models with respect to droplet size and spray penetration for nonevaporating fuel sprays were presented. The study found underestimated droplet sizes for the Kelvin-Helmholtz Rayleigh-Taylor (KHRT) breakup model and hence proposed a new model based on the KH and modified Taylor analogy break-up (MTAB) model to improve the droplet size prediction. A comprehensive review of droplet breakup models has recently been presented by

Jiang et al. (2010). In recent studies by Senecal et al. (2012, 2013) grid convergence for high velocity fuel sprays was investigated using RANS (Senecal et al., 2012) and LES (Senecal et al., 2013) approaches. In both studies, grid sizes down to 32.125 μm were investigated for LPT spray simulation. The authors proposed a cell size of 250 μm for RANS simulation and 62.5–125 μm for LES with respect to accuracy and computational time.

In the present study, the Spray A test case is numerically investigated using LES and LPT methods. As LES in general demands a high mesh resolution, the cell size may reach a critical limit for certain spray submodels. This study presents a comparison of droplet breakup models for four different mesh resolutions. The investigated breakup models are the enhanced Taylor analogy break-up (ETAB) model as proposed by Tanner (1997); Tanner and Weisser (1998), and the Kelvin-Helmholtz Rayleigh-Taylor (KHRT) model by Reitz (1988). The objectives of the study are (i) to investigate the effect of the grid resolution in diesel spray LES, and (ii) to understand the sensitivity of droplet breakup modeling to integral spray quantities and mixture formation. The investigated spray case corresponds to the nonreacting Spray A test case as defined by the ECN and is detailed in Section 3.1. The results, with respect to integral quantities, are quantitatively validated against the experimental data, and the mixture formation is characterized in detail. The added new value of the study in contrast to previous studies on high-velocity fuel sprays using RANS (Abraham and Pickett, 2010; Lucchini et al., 2009; Senecal et al., 2012; Som and Aggarwal, 2010) and LES (Bekdemir et al., 2013; Bharadwaj and Rutland, 2010; Kitaguchi et al., 2012; Senecal et al., 2013) is to (i) carry out simulations on order of magnitude higher mesh resolution, (ii) compare droplet breakup models, and (iii) carry out a mesh sensitivity study.

2. GOVERNING EQUATIONS

2.1 Navier-Stokes Equations

The governing equations for gaseous flows are the compressible Navier-Stokes (NS) equations, describing the conservation of mass (1), momentum (2), energy (3), and species mass fractions (4):

$$\frac{\partial \rho}{\partial t} + \frac{\partial \rho u_j}{\partial x_j} = S_m \tag{1}$$

$$\frac{\partial \rho u_i}{\partial t} + \frac{\partial \left(\rho u_i u_j\right)}{\partial x_j} = \frac{\partial}{\partial x_j}\left(-p\delta_{ij} + \sigma_{ij}\right) + S_i \tag{2}$$

$$\frac{\partial \rho h}{\partial t} + \frac{\partial (\rho h u_j)}{\partial x_j} = \frac{\partial p}{\partial t} + u_j \frac{\partial p}{\partial x_j} + \frac{\partial}{\partial x_j}\left(\lambda \frac{\partial T}{\partial x_j}\right) + S_h \tag{3}$$

$$\frac{\partial \rho Y_k}{\partial t} + \frac{\partial (\rho Y_k u_j)}{\partial x_j} = \frac{\partial}{\partial x_j}\left(\rho D_k \frac{\partial Y_k}{\partial x_j}\right) + S_{Y_k} \tag{4}$$

where ρ, u_i, h, Y_k, T, and p denote the density, velocity component in x_i direction, enthalpy, species mass fractions, temperature and pressure, respectively. The heat conductivity is given by λ and the viscous stress tensor in Eq. (2) is defined as

$$\sigma_{ij} = \mu \left(\frac{\partial u_i}{\partial x_j} + \frac{\partial u_j}{\partial x_i} - \frac{2}{3} \frac{\partial u_i}{\partial x_j} \delta_{ij} \right) \tag{5}$$

where μ is the dynamic viscosity of the fluid. Each equation contains a source term for mass (S_m), momentum (S_i), energy (S_h), and species mass fractions (S_{Y_k}) that incorporates the interaction of the continuous (gas) with the dispersed (liquid) phase.

In LES, Eqs. (1)–(4) are spatially filtered, where the filter can simply be the computational grid and, hence, the filter width can be the grid size. This is a widely used approach, leading to an additional term ($\tilde{\tau}_{\mathrm{SGS}}$) in the filtered NS equations which accounts for the effect of the nonresolved subgrid scales (SGS). Rewriting Eqs. (1)–(4) in the form of $\mathcal{NS} = \mathcal{NS}(\rho, u_i, ...) = S$, the filtered equations can then be written as $\mathcal{NS}(\tilde{\rho}, \tilde{u_i}, ...) = \tilde{S} + \tilde{\tau}_{\mathrm{SGS}}$. The additional term $\tilde{\tau}_{\mathrm{SGS}}$ has to be modeled by a SGS model. Various SGS models have been introduced in literature and have been further discussed by Garnier et al. (2009). In the present setup, the SGS modeling approach is based on the assumption that the grid, or more precisely, the numerical discretization scheme, functions as an implicit low-pass filter and it is assumed that subgrid scales dissipate in the same manner as the numerical scheme. Hence, the nonresolved SGS are not modeled explicitly, which is commonly referred to as *implicit* or no-model LES (Grinstein et al., 2007).

2.2 Droplet Kinematics, Mass and Heat Transfer

Following the LPT approach, the liquid phase is described by several equations for droplet motion, heat, and mass transfer. By defining the droplet Reynolds number

$$\mathrm{Re}_d = \frac{|\vec{u}_g - \vec{u}_d| \, d_d \rho_g}{\mu_g}$$

and the droplet time scale

$$\tau_d = \frac{\rho_d {d_d}^2}{18 \mu_g} \tag{6}$$

the equation of motion reads

$$\frac{d}{dt} \vec{u}_d = \frac{C_D}{\tau_d} \frac{\mathrm{Re}_d}{24} (\vec{u}_g - \vec{u}_d) \tag{7}$$

where the subscript d denotes the droplet and g the gas-phase quantities. The empirically determined values for the drag coefficient C_D can be expressed by the relations

$$C_D = \begin{cases} \dfrac{24}{\mathrm{Re}_d}\left(1 + \dfrac{1}{6}{\mathrm{Re}_d}^{2/3}\right) & \mathrm{Re}_d < 1000 \\ 0.424 & \mathrm{Re}_d \geq 1000 \end{cases}.$$

The change in droplet position is then obtained from

$$\frac{d}{dt}\vec{x}_d = \vec{u}_d.$$

The mass transfer from liquid to gas phase is modeled according to the droplet vaporization correlation by Frössling (1938) and hence the change in droplet mass can be expressed by $(dm_d)/(dt) = -m_d/\tau_e$ with the evaporation time scale

$$\tau_e = \frac{\rho_d {d_d}^2}{6 D_m \,\mathrm{Sh}\, \rho_v \ln\left[(p - p_{v,\mathrm{inf}})/(p - p_{v,s})\right]} \tag{8}$$

The heat transfer at the droplet surface is derived from the droplet energy balance and the Ranz-Marshall correlations for Sherwood (Sh) and Nusselt (Nu) number (Ranz and Marshall, 1952a,b) are applied in the equations for mass and heat transfer. The implementation of the LPT method in OpenFOAM incorporates the parcel approach, which groups physically similar droplets into a parcel and reduces therefore the computational cost significantly.

2.3 Droplet Breakup

Two breakup models, developed and well established for RANS simulations (Stiesch, 2003), are compared in the present study within the implicit LES context.

2.3.1 KHRT Model

The KHRT model was first proposed by Reitz (1988) and is a combination of the Kelvin-Helmholtz (KH) wave model and the assumption of occurring Rayleigh-Taylor (RT) instabilities at the droplet surface. The KH breakup mechanism assumes the droplets to behave like a liquid jet injected into an incompressible gas environment. The liquid surface is therefore subject to small perturbations that are amplified by the liquid–gas phase interaction, which leads to small droplets stripped off from the surface. On the basis of the perturbation growth rate Ω_{KH} and wavelength Λ_{KH} a breakup time and droplet diameter can be determined. Reitz (1988) gives correlation obtained from curve-fits to the analytical solution for the wavelength and growth rate, and the breakup time is then given by

$$\tau_{\mathrm{KH}} = 3.726\, B_1 \frac{r}{\Lambda_{\mathrm{KH}}\Omega_{\mathrm{KH}}} \tag{9}$$

where r denotes the radius of the initial droplets. The RT model is based on theoretical considerations on the stability of liquid–gas interfaces that are accelerated in normal direction. Assuming a linear disturbance growth, a growth rate and wavelength can be determined. The breakup time is then obtained by the reciprocal of the growth rate and a correction factor C_τ to delay the breakup under certain conditions as

$$\tau_{\mathrm{RT}} = C_\tau(1/\Omega_{\mathrm{RT}}) \tag{10}$$

Droplet breakup is encountered if $d_d > \Lambda_{\mathrm{RT}}$ and τ_{RT} is greater than the time of disturbance growth. Both mechanisms, KH and RT, are implemented in a competing manner to determine the droplet breakup.

2.3.2 ETAB Model

Because the ETAB model is based on the Taylor analogy break-up (TAB) model proposed by O'Rourke and Amsden (1987), both models share the basic concept for calculating the breakup time. Following the Taylor analogy, the droplet distortion $y = (2x)/r$, where r is the droplet radius and x the deviation of the droplet equator, can be modeled as a one-dimensional, forced, damped, harmonic oscillator. Hence, the equation of motion reads

$$\ddot{y} + \frac{5\mu_d}{\rho_d r^2}\dot{y} + \frac{8\sigma}{\rho_d r^3}y = \frac{2\rho_g\left(\vec{u}_d - \vec{u}_g\right)^2}{3\rho_d r^2} \tag{11}$$

A solution to Eq. (11) leads to an expression for the distortion y, and the droplets are assumed to break up if y exceeds unity and thus a breakup time can be calculated. In the original TAB model, the radius of the child droplets after breakup is based on an energy balance of the surface and oscillation energy of the parent droplet and the surface and kinetic energy of the child droplet. The ETAB model (Tanner, 1997; Tanner and Weisser, 1998) is a modified version of the TAB model, which aims to predict more realistic results for global spray parameters. Tanner therefore proposed a new method for calculating the number and size of the child droplets after breakup, which assumes the rate of child droplet generation to be proportional to the number of droplets. The constant of proportionality depends on the breakup regime, which is characterized by the Weber number

$$\mathrm{We} = \frac{\rho_g r(\vec{u}_g - \vec{u}_d)^2}{\sigma} \tag{12}$$

In general, the ETAB model computes a greater child radius than the TAB model and results therefore in a more realistic droplet size distribution, especially in the dense spray region close to the nozzle orifice.

2.3.3 Model Constants

Both models include certain constants that are adjusted to match experimental droplet sizes and breakup rates. These empirical constants are well tested in a vast amount of

simulations, where the majority is based on the RANS approach. RANS simulations are usually carried out with fairly large cell sizes (characteristic length of about $\sim$500 μm) [e.g., Kaario et al. (2002, 2003); Reitz (1988); Som and Aggarwal (2010); Tanner (1997); Tanner and Weisser (1998)], and the models have not been tested much for LES as noted by Bharadwaj and Rutland (2010). A detailed description of these constants is given in the original publications by Reitz (1988) and Tanner (1997). In this study, the model constants are set to their default value as listed in Tables 1 and 2.

3. SPRAY CONDITIONS AND COMPUTATIONAL SETUP

3.1 Spray A Conditions

The simulation in the present study are carried out for the Spray A test case as specified by the ECN. The conditions therefore correspond to the experimental data obtained at the Sandia National Laboratories, USA and are detailed in the following. The ambient gas density and temperature for Spray A are 22.8 kg/m^3 and 900 K, respectively. For the nonreacting setup, a preburn chamber is used with 0% oxygen content. The injected fuel is n-dodecane ($\mathrm{C_{12}H_{26}}$) in order to resemble a diesel-like fuel spray, and the nominal injection pressure is 150 MPa. The nominal nozzle diameter of the injector is $D_{inj} = 90$ μm, and the discharge coefficient was experimentally determined to be 0.86, leading to an average injection velocity $U_{inj} \approx 590$ m/s. In Fig. 1, the injection mass flow rate measured at Sandia National Laboratories is shown.

3.2 Numerical Methods and Mesh

The simulations are carried out using the open-source CFD tool box OpenFOAM developed by OpenCFD Ltd (2012). The simulation approach is based on a compressible flow solver with an implicit pressure treatment based on the PISO-algorithm. The spatial accuracy of the code is formally second order, and an implicit, second-order accurate time integration is used.

TABLE 1: KHRT model constants

B_0	B_1	C_τ	C_{RT}	ms_{Lim}	$\mathrm{We}_{\mathrm{Lim}}$
0.61	40	1	0.1	0.03	6

TABLE 2: ETAB model constants

C_μ	C_Ω	$\mathrm{We}_{\mathrm{Crit}}$	k_1	k_2	$\mathrm{We}_{\mathrm{Trans}}$
10	8	12	0.2	0.2	100

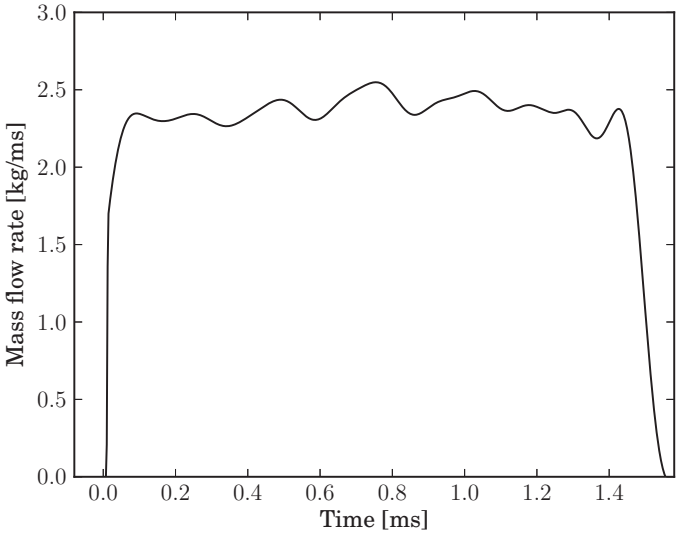

FIG. 1: Mass flow rate corresponding to the experiments at Sandia National Laboratories, USA

The geometry of the computational domain resembles the combustion vessel at Sandia National Laboratories, for which the experimental validation data are obtained. A fully hexahedral base mesh is used, which is refined by a 2:1 cell-splitting approach in the spray region in order to properly resolve the flow details. Four mesh resolutions are applied in this study with minimum cell sizes of 41.67, 62.5, 125, and 250 μm and respective cell counts of approximately 16.2, 4.6, 1.2, and 0.8 million. A visualization of the computational mesh is given in Fig. 2, showing the refinement levels and a wireframe representation. From the base mesh with a characteristic cell size of 250 μm (Fig. 2, gray), the 125 and 62.5 μm meshes are obtained by adding respective refinement regions. The 41.67 μm mesh has the same refinement structure as the 62.5 μm mesh. With respect to the spray characteristics known from the experimental results, the extent of the refinement regions is set to cover the main region of interest.

3.3 Spray Initial and Boundary Conditions

It is a common difficulty in LES/LPT modeling to estimate the droplet size range for the initial droplet size distribution (IDSD). This problem arises typically due to the absence of quantitative experimental droplet size measurements. However, there are other indirect ways to estimate the droplet size range. In the high-temperature conditions of Spray A, the experimental sprays appear visually as a mist already near the nozzle exit. If this mist consist of droplets below supercritical conditions, then these droplets are likely to be very small $d \ll D_{inj}$ due to the visual arguments and also the high-injection

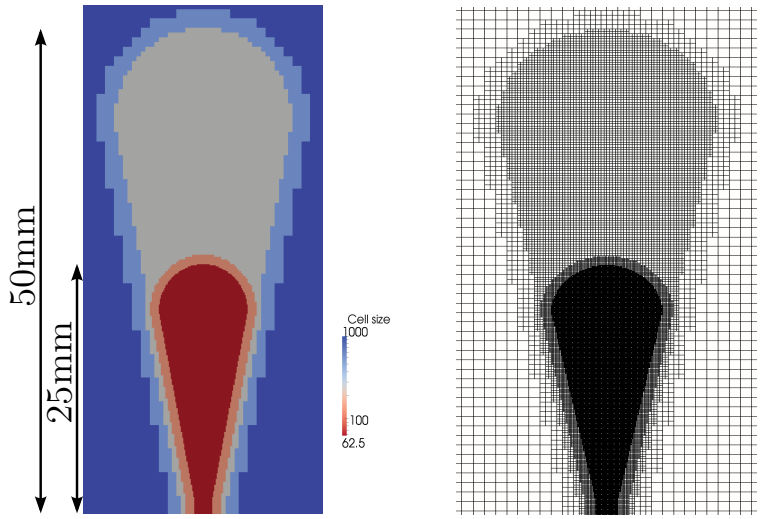

(a) (b)

FIG. 2: (a) Computational mesh with refinement regions and (b) wireframe representation.

pressures (Pickett et al., 2010). However, it has even been proposed that the fuel could be in supercritical state, where a discrete liquid phase does not exist (Dahms et al., 2013). In general, one could also deduce the droplet size by considering the interaction between droplets with the surrounding turbulence. Hillamo et al. (2010) studied nonevaporating fuel sprays observing clear interaction of droplets with the surrounding turbulence in the immediate vicinity of the nozzle exit $z < 10D_{inj}$. Because only small droplets with Stokes number St $\ll 1$ are known to interact with turbulent eddies with characteristic velocity scale U and time scale T, Hillamo et al. (2010) were able to deduce the presence of significant amounts of very small droplets. In the present study, we model Spray A by assuming that the mist, as visualized by the Sandia researchers, consists of small droplets that are still below the supercritical temperatures. We note that, in reality, it could be possible that both sub- and supercritical phases exist in the dense spray regime. The droplet size range is modeled by assuming that the maximum droplet size $D_{\max} = D_{inj}/5 = 18$ μm, whereas the minimum droplet size $D_{\min} = D_{inj}/90 = 1$ μm. This choice is somewhat arbitrary but, noting that the gas-phase velocity in the injector vicinity can be estimated to $U_{inj,g} \approx 0.4 \cdot U_{inj}$ = 236.0 m/s, the size range still corresponds to an unstable regime, where the maximum Weber number range 50–1500 indicates rapid secondary atomization near the injection position (Stiesch, 2003). The droplet size range is also still large enough that the droplets do not evaporate immediately. The IDSD is then modeled by resorting to the Rosin-Rammler distribution function, which is widely used in multidimensional spray modeling. The

TABLE 3: Rosin-Rammler distribution parameters

$D_{\max}$	$D_{\min}$	d	n
18 μm	1 μm	6 μm	3

used IDSD parameters are summarized in Table 3 and lead to an initial Sauter mean diameter (SMD) of ≈6 μm. On the basis of our numerical experiments, this IDSD may provide results relatively close to the experiments as discussed in what follows.

The high injection velocity and the low droplet time scale τ_d in combination with the small cell sizes require a small time step which was set to $\Delta t = 2 \times 10^{-8}$ s for the 250, 125, and 62.5 μm mesh resolutions and to $\Delta t = 1 \times 10^{-8}$ s for the 41.67 μm mesh resolution.

4. RESULTS AND DISCUSSION

4.1 Global Spray Characteristics

Figure 3 shows an instantaneous visualization of Spray A based on the present LES from a further developed state. Figure 3 shows several general features characteristic to Spray A and high-velocity fuel sprays:

1. Breakup length: The distance from the injection location until which the droplets reach a stable diameter and no further breakup occurs.

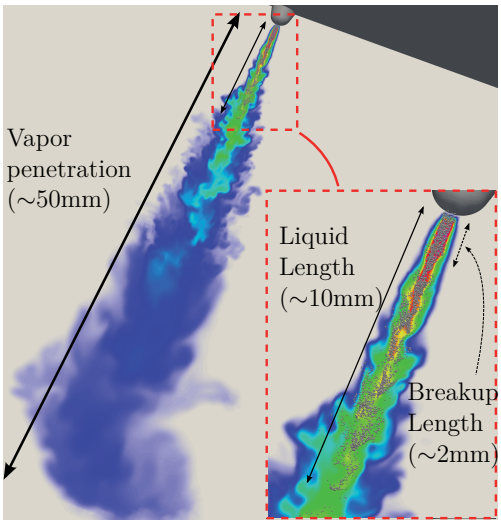

FIG. 3: Visualizations of Spray A from LES data: Indicated are several length scales relevant to fuel sprays, mixture formation, and combustion.

2. Liquid length: The maximal penetration of the liquid phase. The liquid length marks the steady state at which the total evaporation rate equals the fuel injection rate.

3. Vapor penetration: The maximum distance to the injection location of 0.1% vapor mass fraction

The investigated spray case in the present study is characterized by a high injection pressure and small nozzle hole diameter, resulting in a high injection velocity and mass flow rate. In combination with the high ambient gas temperature and density, fast atomization and evaporation is characteristic for the present spray case and, thus, a short liquid length is observed in the experimental results. Concerning the spray development, it is seen from the experimental data that a concurrent liquid and vapor penetration of 8 mm is reach in only 0.04 ms, after which a separation of vapor and liquid penetration is observed. The liquid length (10.5 mm) is then reached at $t \approx 0.23$ ms.

The liquid length denotes in many aspects an important quantity with respect to mixture formation and combustion, as the liquid phase is not only the source for the fuel vapor but also turbulence generation. The penetration and evaporation of the liquid fuel leads further to a significant cooling of the surrounding gas phase. The simulated liquid length is compared to the experimental data obtained at the Sandia National Laboratories in Fig. 4. In the computational setup, the liquid length is defined as the maximum distance of 95% liquid mass to the injection location. As a first observation, it can be seen that the cases with a 250 µm mesh resolution are not able to correctly predict the liquid length. The situation improves significantly for the 125 µm mesh resolution, which leads in the case of the ETAB model to an accurate prediction of the liquid length and

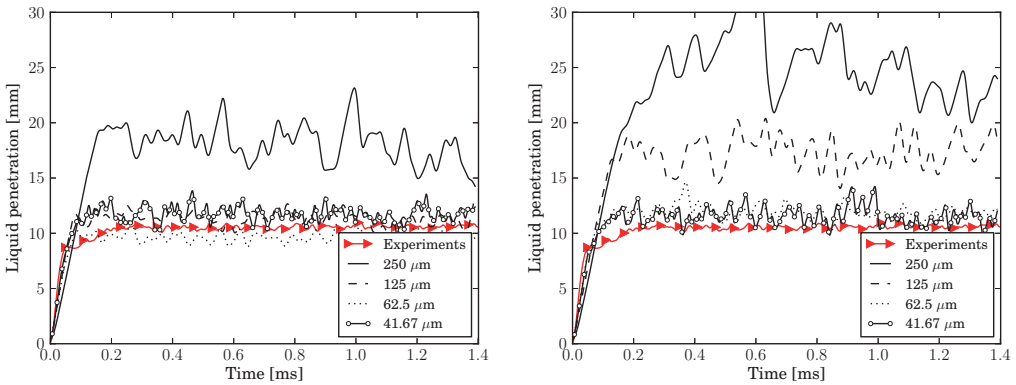

(a) ETAB (b) KHRT

FIG. 4: Liquid length versus time for the four mesh sizes comparing the ETAB and KHRT breakup model.

for the KHRT model to an overshoot by ≈5 mm. The simulations with the 41.67 and 62.5 μm mesh resolution provide good results, which appear to be insensitive to the breakup model.

From further investigations of the 3D flow field (Fig. 5) for the 250 μm mesh resolution can be concluded that the cell size is too large to model the momentum transfer from liquid to gas phase correctly or to capture the turbulent motion of the flow. Hence, also the air entrainment and, consequently, the heat transfer from the gas phase to the droplets is not captured correctly. Both effects contribute to a slower evaporation and, thus, the significantly overpredicted liquid length. Even though the liquid length for the 125 μm–KHRT case is also overpredicted, the mesh resolution is high enough to resolve a considerable part of the turbulent fluctuations and hence deeper investigations are required. Therefore, the following investigations will not consider the cases with a 250 μm mesh resolution and focus only on the 125, 62.5, and 41.67 μm mesh resolutions. To gain a better understanding of the spray behavior and turbulence generation, the gas-phase velocities are analyzed in the following section.

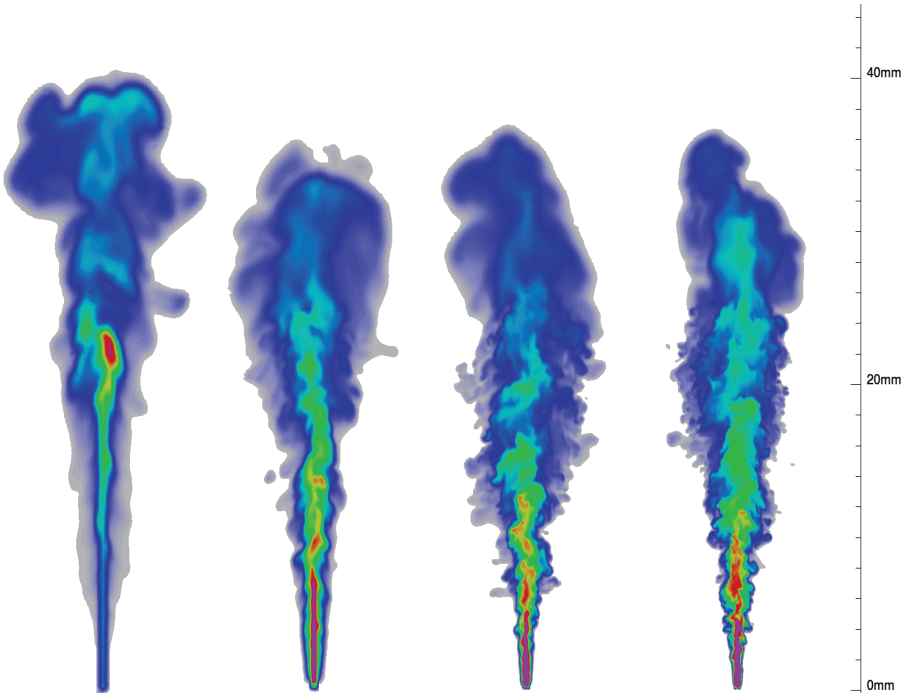

FIG. 5: Instantaneous vapor mass fraction comparing the four mesh resolutions (KHRT model).

4.2 Gas-Phase Velocities

Figure 6 shows the gas-phase velocity along the spray centerline in the fully developed state (t = 1.4 ms). A strong acceleration of the gas phase starting at the injection location till the maximum velocity is reached at a distance of ≈5 mm from the injection location. This acceleration is observed for all four considered cases, where the maximum velocities are in the range of 300–350 m/s. The acceleration phase is followed by a deceleration, where the centerline velocity decays as $|\vec{u}| \sim 1/z$, which is clearly seen in the log-log representation [Fig. 6(b)]. Similar axial velocity decays are observed for gas jets emphasizing the similarities of high injection-pressure fuel sprays to gas jets (Iyer and Abraham, 1997; Vuorinen et al., 2010a,b, 2011). Because the gas phase is mainly accelerated due to drag forces resulting from the injected droplets, the centerline velocity indicates how well the momentum transfer from liquid to gas phase is captured in the simulation.

Where the former observations are made for a fully developed state at later time (t = 1.4 ms), similar characteristics are found at earlier times. In fact, the maximum value of the gas-phase velocity is reached in <0.2 ms, resulting from the steep rise in the mass flow profile and the overall high injection velocity. Hence, the spray approaches a developed state already at earlier times and is further characterized by a steady liquid length, while the vapor penetration is steadily increasing. The time evolution of the instantaneous gas-phase velocity for the 41.67 μm mesh resolution is shown in Fig. 7, comparing the ETAB and KHRT breakup model. Here, the transient and unsteady features of the flow are clearly noted and it is seen that with both breakup models the turbulent characteristics of the flow can be reproduced well.

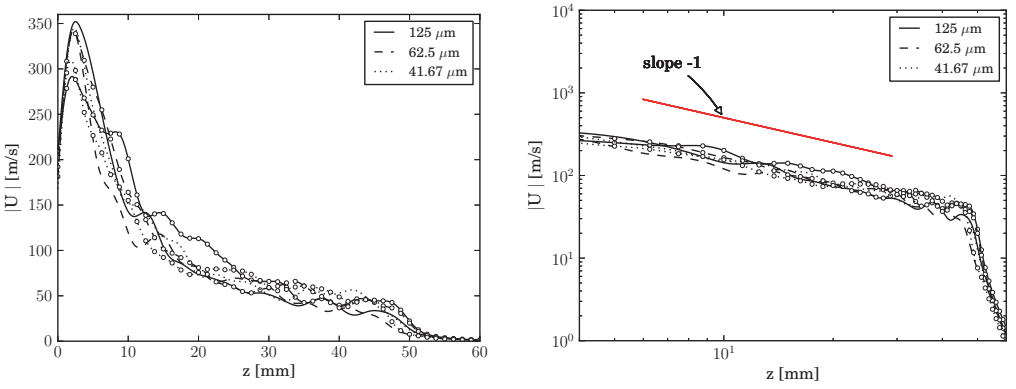

FIG. 6: Gas-phase velocity along the spray centerline. (b) illustrates the gas jet analogy by showing the $1/z$-decay of gas phase velocity on a log-log scale; KHRT: ○, ETAB: no marker

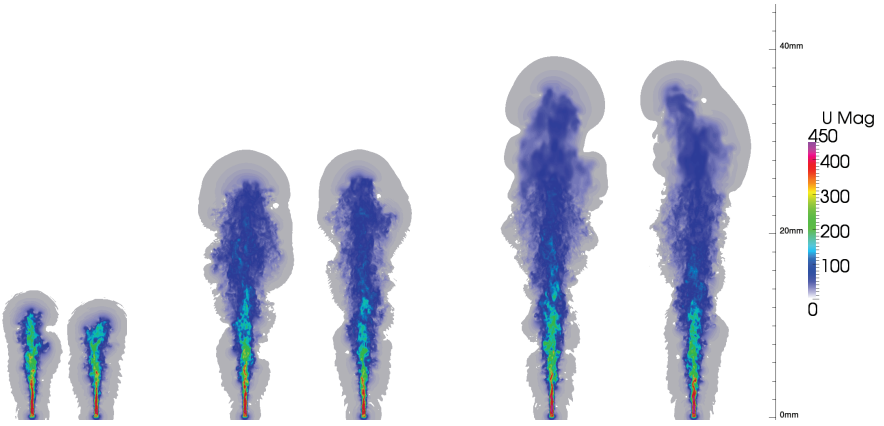

(a) 0.1ms (b) 0.4ms (c) 0.7ms

FIG. 7: Evolution of the instantaneous gas phase velocity comparing the ETAB (left) and KHRT (right) model for the 41.67 μm mesh resolution.

Until now only local characteristics have been analyzed because they are important for the spray development. However, to compare the velocity results at a global scale, the probability density function (PDF) of specific kinetic energy $\left(e_{kin} = (1/2)\rho_g {U_g}^2\right)$ is analyzed for the whole spray. Considering a fully developed state at t = 1.4 ms, the PDF (e_{kin}) shows that the volume containing a high kinetic energy is very low compared to the overall volume of accelerated gas (Fig. 8). The same trend is seen for all cases as the volume of high kinetic energy decays rapidly with increasing kinetic energy.

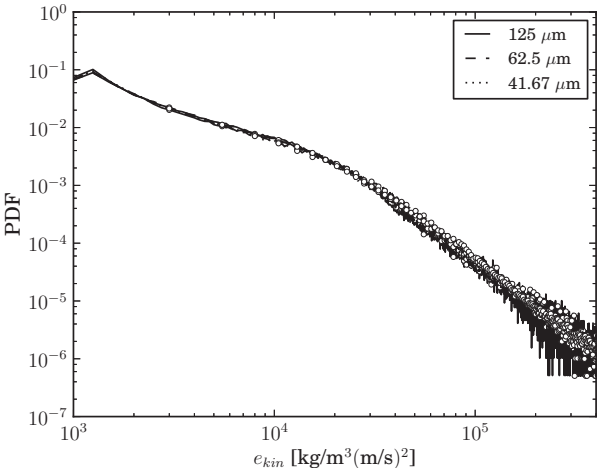

FIG. 8: Probability density of specific kinetic energy e_{kin} at time t = 1.4 ms on a log-log scale; KHRT: ○, ETAB: no marker

4.3 Droplet Quantities

The mass averaged droplet velocity along the spray centerline behaves for the six cases similarly: After a steep drop close to the injection location, the velocity decays linearly until the liquid length is reached (Fig. 9). Also in this plot the higher liquid length for the 125 μm–KHRT case is clearly noted. A commonly used measure for the averaged droplet sizes is given by the Sauter Mean Diameter

$$\text{SMD} = \sum_{i=1}^{N} {d_i}^3 \Big/ \sum_{i=1}^{N} {d_i}^2$$

The SMD computed for the whole spray is nearly constant during the steady-state phase of the liquid length. Significant differences are observed between the two breakup models, as the ETAB model predicts a lower SMD of approximately 0.4 μm (125 and 62.5 μm) and 0.3 μm (41.67 μm) compared to the KHRT, which leads to 1.4, 1.2, and 1.1 μm for the 125, 62.5, and 41.67 μm mesh resolution, respectively.

The PDF of droplet diameter (Fig. 10) shows a clear peak for the ETAB cases, indicating a rather uniform size distribution. The KHRT cases show a broader range of droplet sizes and a higher mean value, which is in line with the SMD values. The reason for these differences can be attributed to the KH wave model as it strips off small droplets from the parent droplet. Given the overall small diameter of the parent droplet, the even smaller child droplets will evaporate almost instantaneously because the evaporation time scale is proportional to the square of the diameter: $\tau_e \sim d^2$ [compare Eq. (8)], as is also the higher SMD for the KHRT cases, as the droplet lifetime of child droplets is very

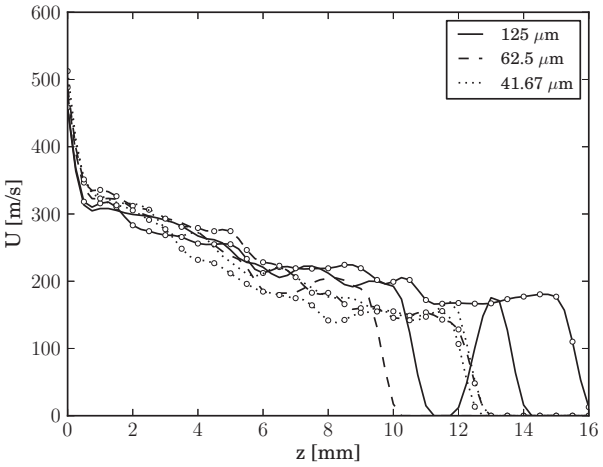

FIG. 9: Mass averaged droplet velocity along the spray centerline; KHRT: ○, ETAB: no marker

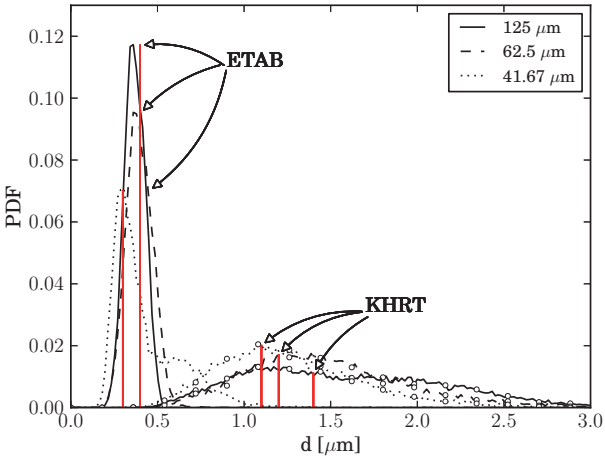

FIG. 10: Probability density function of droplet diameter at time t = 1.4 ms; vertical bars indicate the corresponding SMD; KHRT: ○, ETAB: no marker

small. An analysis of the Weber number as a function of droplet penetration (Fig. 11) suggests that the droplet breakup occurs mainly within 2 mm from the injection location. Hence, the droplet lifetime is determined by the evaporation rate (i.e., evaporation time scale). Given a rather constant injection pressure (i.e., initial droplet velocity), the limiting factor for the liquid length is therefore the evaporation time scale. It should be mentioned that for the present Spray A simulation, boiling conditions do not occur due

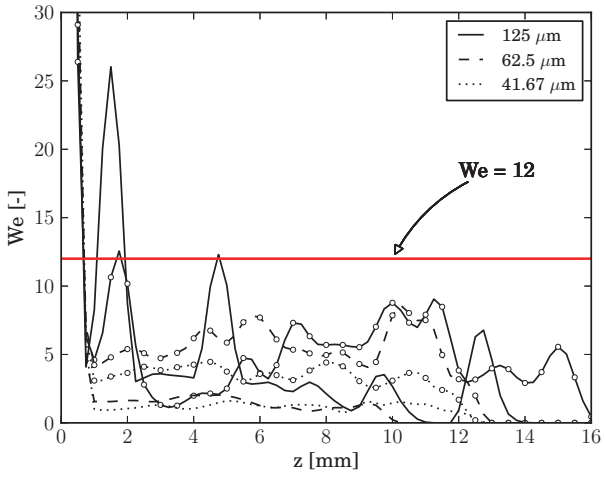

FIG. 11: Weber number along the spray centerline at time t = 1.4 ms; KHRT: ○, ETAB: no marker

to the high ambient pressure. However, the evaporation time scale is, besides the droplet diameter, dependent on the temperature and thus heat transfer from gas to liquid phase. The rate of heat transfer again is limited by air entrainment (i.e. mixing), which suggests further analysis of the gas phase/vapor quantities.

4.4 Vapor Distribution

The instantaneous vapor mass fractions are visualized in Fig. 12 at three instants of time for the 41.67 μm mesh resolution. At each instance of time, the ETAB and KHRT are compared. Significant differences are observed in the near-nozzle region, showing a higher vapor mass fraction for the KHRT model. These differences can be explained by the small, quickly evaporating droplets stemming from the KH wave model as stated in Section 4.3. However, given an adequate mesh resolution, both models are able to capture the characteristic, turbulent features of the spray (e.g., the Kelvin-Helmholtz waves at the vapor–gas interface).

To quantify the differences seen in Fig. 12 the vapor mass fraction along the spray centerline is shown in Fig. 13. For the ETAB cases, (i) very little or no differences are observed between the mesh resolutions and (ii) the peak values occur at the end of the liquid length at ∼10 mm. The graphs for the KHRT cases show the steep rise and the high peak values in the injector vicinity, where the peak value for the 125 μm mesh resolution is significantly higher than for the 62.5 and 41.67 μm mesh resolution. However, it is also seen that the vapor mass fraction for the considered cases approach each other after the

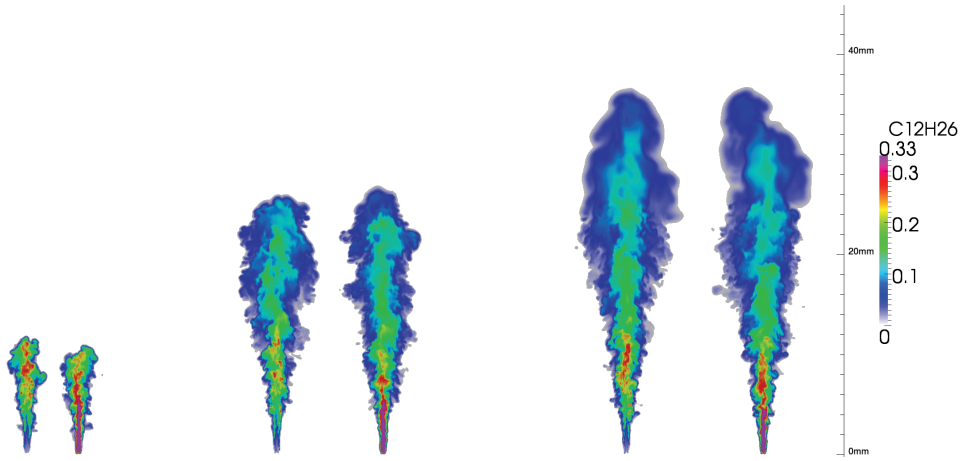

(a) 0.1ms (b) 0.4ms (c) 0.7ms

FIG. 12: Evolution of the instantaneous vapor mass fraction comparing the ETAB (left) and KHRT (right) model for the 41.67 μm mesh resolution.

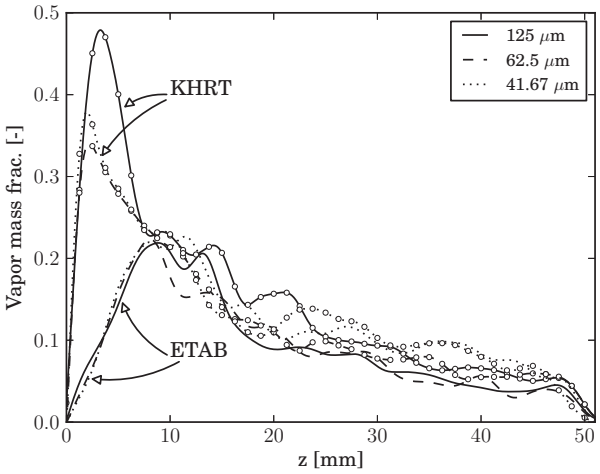

FIG. 13: Vapor mass fraction along the spray centerline at time t = 1.4 ms; KHRT: ○, ETAB: no marker

liquid phase has been evaporated. For the 125 μm–KHRT case, fluctuations are observed in a range between 10 and 25 mm as the liquid fuel is still present until 15–20 mm.

On the basis of Fig. 12, there is a clear qualitative similarity seen in vapor distribution for the KHRT and ETAB breakup model. Similar to what was shown in Section 4.2 for the PDF (e_{kin}), we next consider the PDF of vapor mass fraction estimated over the whole spray volume (Fig. 14), where the spray volume is defined by a vapor mass fraction of $>$0.1%. Similar to the mixing analysis presented in Vuorinen et al. (2013),

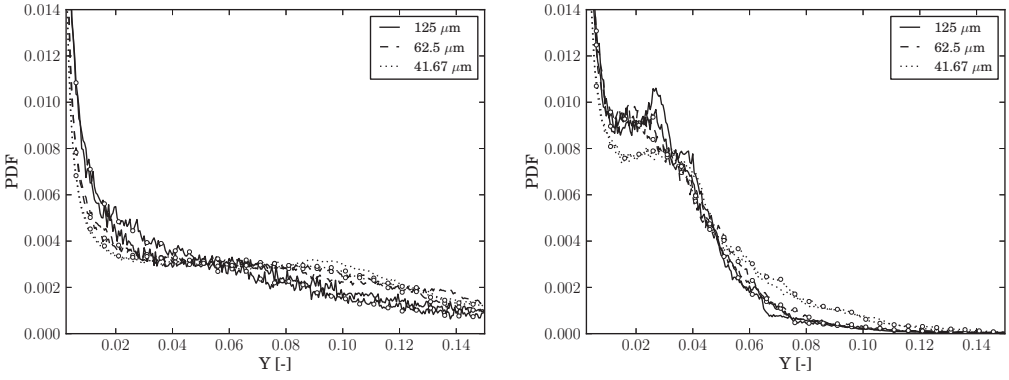

(a) (b)

FIG. 14: Time evolution for the probability density function of the vapor mass fraction (Y); KHRT: ○, ETAB: no marker

PDFs at two time instants, one at an early (t = 0.2 ms) and one at a later state (t = 1.4 ms) when the vapor is penetrated further are investigated. The results show a similar behavior for both breakup models at all mesh resolutions. It is seen that the mixing increases similarly for the 125 and 62.5 μm cases as the probability for the lower vapor mass fractions becomes higher in the later stage. However, in case of the 41.67 μm mesh resolution a higher probability for rich mixture is observed compared to the 125 and 62.5 μm cases is observed, indicating a slower mixing process. This result is also in line with the computed radial vapor profiles shown later.

A comparison of the experimental and simulated radial vapor mass fraction profiles at 25 mm distance to the injection location is shown in Fig. 15. The simulation with 125 and 62.5 μm mesh resolution are not able to match the experimental profiles, as the vapor mass fraction in the center is under-predicted and the spreading of the spray overpredicted. However, for the 41.67 μm mesh resolution, a better agreement with the experimental data is achieved, as the vapor mass fraction in the center is closer to experiments. These findings are in agreement with the results for the PDF of the vapor mass fraction. However, the results for the radial profiles show a high dependency on the breakup models and mesh resolutions and, hence, a reproduction of the experimental results appears to be difficult for a single LES realization. Similar findings were presented in Senecal et al. (2013) and Abraham and Pickett (2010), where the latter study also found a strong dependence of mixing on the initial SMD. However, the effect of the initial SMD was not studied in the present work.

A comparison of the experimental and the simulated vapor penetration is shown in Fig. 16. The vapor penetration is defined from 0.1% vapor mass fraction contour. The results for the vapor penetration are in good agreement with the experimental data.

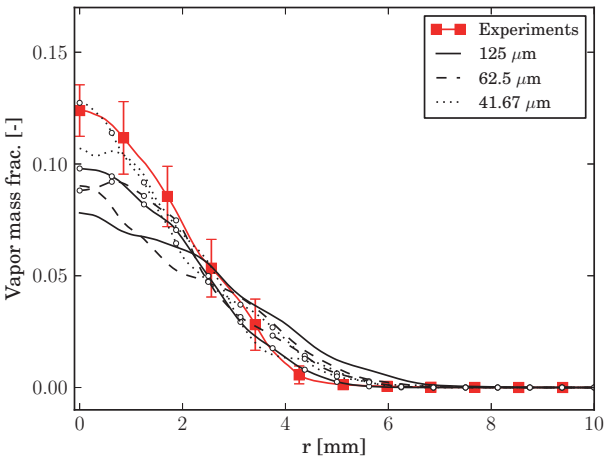

FIG. 15: Radial vapor mass fraction profiles at a distance of z = 25 mm; KHRT: ○, ETAB: no marker

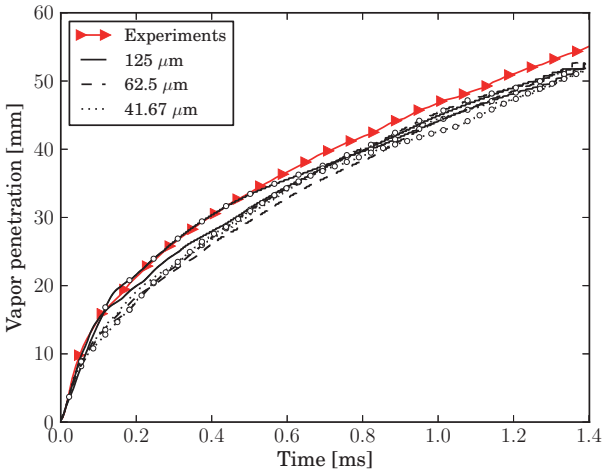

FIG. 16: Vapor penetration over time; KHRT: ○, ETAB: no marker

However, it is observed that the simulations slightly underpredict the vapor penetration. The marginally higher vapor penetration of the 125 μm cases compared to the 62.5 and 41.67 μm cases in the early stage ($t < 0.6$ ms) can be attributed to the higher liquid penetration. In the later stage, the penetration curves collapse nearly to a single line. The results concerning the vapor distribution furthermore underline the similarities between high momentum sprays and gas jets, as well as the requirement for a high mesh resolution. This is especially true for the KHRT model due to the high fuel vapor mass fraction in the injector vicinity.

4.5 Energy Spectra

Finally, to asses the quality of the LES, the energy spectra are an important measure. The PSD of the kinetic energy is shown for the ETAB [Fig. 17(a)] and KHRT [Fig. 17(b)] model, comparing the four mesh resolutions. The velocity probes are taken at 7 mm distance to the injection location and 1 mm off the spray centerline. In general, it is seen that a range of frequencies is resolved with the present simulation setup for all mesh resolutions. Ideally, all the spectra should overlap to reach grid independence. However, as already seen in the results for velocity and vapor distribution, the results are changing significantly with the mesh resolution. Hence, also several differences in the energy spectra are noted, as follows:

1. The spectra for the 250 and 125 μm mesh resolution fall down rapidly, indicating that the resolved energy decays fast with an increasing frequency.

2. The energy contained in the low frequencies is highest for the 250 μm mesh resolution.

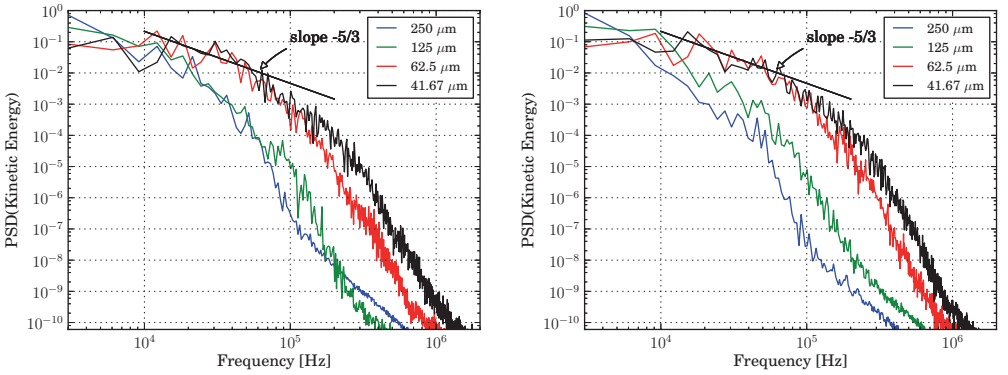

FIG. 17: Kinetic energy spectra for the four mesh sizes comparing the ETAB and KHRT breakup model.

3. For the 62.5 and 41.67 μm mesh resolution, the spectra are overlapping up to a frequency of $\approx 2 \times 10^5$ Hz. At higher frequencies, a slightly higher energy content for the cases with a 41.67 μm mesh resolution is found. However, the resolved energy decays in the same manner for both mesh resolutions.

5. CONCLUSIONS

In the present work, LES of the ECN target conditions Spray A, a high-velocity fuel spray, are presented. The simulations have been carried out at four computational mesh resolutions using the implicit LES approach and LPT. Compared are two breakup models and their effect on local and global spray characteristics. The findings of the study are summarized in the following:

1. The implicit LES approach in combination with LPT is capable of capturing the characteristic features of a high-velocity fuel spray, given a sufficient mesh resolution.

2. A higher mesh resolution, and hence an increase in the resolved turbulent scales, lead to better results, especially regarding the mixing formation. With respect to the mixing controlled nature of high-velocity fuel sprays, this further emphasizes the requirement for an adequate mesh resolution.

3. An adequate mesh resolution for the present spray case was found when cell sizes are on the order of the nozzle hole diameter or smaller.

4. Significant differences between the ETAB and KHRT breakup models were observed with respect to droplet size and local evaporation rate. Also, the vapor mass distribution was different in the spray region where liquid fuel was still present.

5. The global spray characteristics are shown to be rather insensitive to the breakup modeling approach. This holds also true for the local mixture formation after the liquid phase has been evaporated, and hence, the resulting gas jets are very similar.

From the viewpoint of LES fuel spray modeling, it can be argued that with the increase in mesh resolution and the resulting resolved features of the flow, the importance of the breakup modeling decreases. Research on fuel sprays has traditionally been relying on the RANS approach, where cell sizes much larger than the nozzle hole diameter are used. The lower mesh resolution and the nature of the RANS approach to give a time-averaged image of the flow require a higher degree of modeling for the liquid phase. Hence, the importance of the breakup modeling to account for certain phenomena is higher in order to predict the global spray characteristics correctly. This dependency vanishes in high-resolution LES, even though atomization and droplet breakup still has to be accounted for.

ACKNOWLEDGMENTS

The financial support by the Finnish Funding Agency of Technology and Innovation (Tekes) within the Cleen SHOK project Future Combustion Engine Power Plant (FCEP) is deeply acknowledged. The authors also thank the Finnish IT Center for Science (CSC) for providing the computational resources.

REFERENCES

Abraham, J. and Magi, V., A virtual liquid source (VLS) model for vaporizing diesel sprays, *SAE Tech. Paper No. 1999-01-0911*, 1999.

Abraham, J. and Pickett, L. M., Computed and measured fuel vapor distribution in a diesel spray, *Atomization Sprays*, vol. **20**, no. 3, pp. 241–250, 2010.

Bekdemir, C., Somers, L., de Goey, L., Tillou, J., and Angelberger, C., Predicting diesel combustion characteristics with large-eddy simulations including tabulated chemical kinetics, *Proc. Combust. Inst.*, vol. **34**, no. 2, pp. 3067–3074, 2013.

Bharadwaj, N. and Rutland, C. J., A large-eddy simulation study of sub-grid two-phase interaction in particle-laden flows and diesel engine sprays, *Atomization Sprays*, vol. **20**, no. 8, pp. 673–695, 2010.

Dahms, R. N., Manin, J., Pickett, L. M., and Oefelein, J. C., Understanding high-pressure gas-liquid interface phenomena in Diesel engines, *Proc. Combust. Institute*, vol. **34**, no. 1, pp. 1667–1675, 2013.

Engine Combustion Network (ECN), "Spray A" Operating Condition, Aug. 2012; http://http://www.sandia.gov/ecn/.

Frössling, N., Über die Verdunstung fallender Tropfen, *Gerlands Beiträge Geophys.*, vol. **52**, pp. 170–216, 1938.

Garnier, E., Adams, N., and Sagaut, P., *Large Eddy Simulation for Compressible Flows*, Scientific Computation, Springer, New York, 2009.

Grinstein, F. F., Margolin, L. G., and Rider, W. J., *Implicit Large Eddy Simulation*, Cambridge University Press, New York, 2007.

Hillamo, H., Sarjovaara, T., Kaario, O., Vuorinen, V., and Larmi, M., Diesel spray visualization and shockwaves, *Atomization Sprays*, vol. **20**, no. 3, pp. 177–189, 2010.

Iyer, V. and Abraham, J., Penetration and dispersion of transient gas jets and sprays, *Combust. Sci. Technol.*, vol. **130**, nos. 1–6, pp. 315–334, 1997.

Jiang, X., Siamas, G., Jagus, K., and Karayiannis, T., Physical modelling and advanced simulations of gasliquid two-phase jet flows in atomization and sprays, *Prog. Energy Combust. Sci.*, vol. **36**, no. 2, pp. 131–167, 2010.

Kaario, O., Larmi, M., and Tanner, F. X., Non-evaporating liquid spray simulations with the ETAB and WAVE droplet breakup models, *18th Annual Conf. on Liquid Atomization & Spray Systems*, *ILASS-Europe*, Zaragoza, Spain, 9–11 September 2002.

Kaario, O., Pokela, H., Kjäldman, L., Tiainen, J., and Larmi, M., LES and RNG turbulence modeling in DI diesel engines, *SAE Tech. Paper No. 2003-01-1069*, 2003.

Kitaguchi, K., Hatori, S., Hori, T., and Senda, J., Optimization of breakup model using les of diesel spray, *Atomization Sprays*, vol. **22**, no. 1, pp. 57–77, 2012.

Lucchini, T., DErrico, G., Ettorre, D., and Ferrari, G., Numerical investigation of non-reacting and reacting diesel sprays in constant-volume vessels, *SAE Int. J. Fuels Lubr.*, vol. **2**, no. 1, pp. 966–975, 2009.

Meijer, M., Somers, B., Johnson, J., Naber, J., Lee, S.-Y., Malbec, L. M., Bruneaux, G., Pickett, L. M., Bardi, M., Payri, R., and Bazyn, T., Engine combustion network (ECN): Characterization and comparison of boundary conditions for different combustion vessels, *Atomization Sprays*, vol. **22**, no. 9, pp. 777–806, 2012.

OpenCFD Ltd, OpenFOAM, Dec. 2012; http://www.openfoam.com.

O'Rourke, P. J. and Amsden, A. A., The TAB method for numerical calculation of spray droplet breakup, *SAE Tech. Paper No. 872089*, 1987.

Payri, R., García-Oliver, J. M., Bardi, M., and Manin, J., Fuel temperature influence on diesel sprays in inert and reacting conditions, *Appl. Thermal Eng.*, vol. **35**, pp. 185–195, 2012a.

Payri, R., Salvador, F. J., Gimeno, J., and García, A., Flow regime effects over non-cavitating diesel injection nozzles, *Proc. Mech. Eng., Part D*, vol. **226**, no. 1, pp. 133–144, 2012b.

Pickett, L. M., Genzale, C. L., Bruneaux, G., Malbec, L.-M., Hermant, L., Christiansen, C., and Schramm, J., Comparison of diesel spray combustion in different high-temperature, high-pressure facilities, *SAE Tech. Paper No. 2010-01-2106*, vol. **3**, no. 2, pp. 156–181, 2010.

Ranz, W. E. and Marshall, W. R. J., Evaporation from drops, Part I, *Chem. Eng. Prog.*, vol. **48**, no. 3, pp. 141–146, 1952a.

Ranz, W. E. and Marshall, W. R. J., Evaporation from drops, Part II, *Chem. Eng. Prog.*, vol. **48**, no. 3, pp. 173–180, 1952b.

Reitz, R. D., Modeling atomization processes in high-pressure vaporizing sprays, *Atomisation Spray Technol.*, vol. **3**, pp. 309–337, 1988.

Senecal, P. K., Pomraning, E., Richards, K. J., and Som, S., Grid-convergent Spray Models for Internal Combustion Engine CFD Simulations, *Proc. of ASME 2012 Internal Combustion Engine Division Fall Technical Conf.*, Paper No. iCEF2012-92043, 2012.

Senecal, P. K., Pomraning, E., Richards, K. J., and Som, S., An investigation of grid convergence for spray simulations using an LES turbulence model, *SAE Tech. Paper No. 2013-01-1083*, 2013.

Siebers, D. L., Liquid-phase fuel penetration in diesel sprays, *SAE Technical Paper No. 980809*, 1998.

Som, S. and Aggarwal, S. K., Effects of primary breakup modeling on spray and combustion characteristics of compression ignition engines, *Combust. Flame*, vol. **157**, no. 6, pp. 1179–1193, 2010.

Stiesch, G., *Modeling Engine Spray and Combustion Processes*, Springer, New York, 2003.

Tanner, F. X., Liquid jet atomization and droplet breakup modeling of non-evaporating diesel fuel sprays, *SAE Tech. Paper No. 970050*, 1997.

Tanner, F. X. and Weisser, G., Simulation of liquid jet atomization for fuel sprays by means of a cascade drop breakup model, *SAE Tech. Paper No. 980808*, 1998.

Vuorinen, V., Hillamo, H., Kaario, O., Larmi, M., and Fuchs, L., Large eddy simulation of droplet Stokes number effects on turbulent spray shape, *Atomization Sprays*, vol. **20**, no. 2, pp. 93–114, 2010a.

Vuorinen, V., Hillamo, H., Kaario, O., Nuutinen, M., Larmi, M., and Fuchs, L., Large eddy simulation of droplet Stokes number effects on mixture quality in fuel sprays, *Atomization Sprays*, vol. **20**, no. 5, pp. 435–451, 2010b.

Vuorinen, V., Hillamo, H., Kaario, O., Nuutinen, M., Larmi, M., and Fuchs, L., Effect of droplet size and atomization on spray shape: A priori study using large-eddy simulation, *Flow Turb. Combust.*, vol. **86**, pp. 533–561, 2011.

Vuorinen, V., Yu, J., Tirunagari, S., Kaario, O., Larmi, M., Duwig, C., and Boersma, B. J., Large-eddy simulation of highly underexpanded transient gas jets, *Phys. Fluids*, vol. **25**, no. 1, paper 016101, 2013.